THE JOURNAL OF PHYSICAL CHEMISTRY C
A JOURNAL OF THE AMERICAN CHEMICAL SOCIETY

pubs.acs.org/JPCC
Article

Dynamics of Palladium and Palladium–Gold Thin-Film Catalysts during Acetylene Semihydrogenation Revealed by Synchrotron Grazing Incidence X-ray Diffraction

Albert Gili,* Lukas Thum, Meysam Khodabakhshi, Shivam Shivam, Raul Garcia-Diez, Marcus Bär, Markus Wollgarten, Rutger Schlatmann, and Daniel Amkreutz

Cite This: J. Phys. Chem. C 2025, 129, 13312–13321

ABSTRACT: Catalytic thin films are an exciting concept in the field of heterogeneous catalysis that produce 2D structures with precisely engineered active sites to generate fundamental knowledge and optimize catalytic performance. Acetylene semihydrogenation on Pd catalysts is an industrially crucial chemical reaction known for its complex subsurface chemistry: competitive occupation of the metal's interstitials between atomic hydrogen and carbon leads to substantial changes in reaction selectivity, the key performance indicator. In the present work, we monitor the dynamics of supported thin films of Pd and PdAu during the reaction using a combination of synchrotron *in situ* GIXRD, pre- and post-reaction XPS and TEM. PdH_x formation occurs at room temperature, with a significant increase in the lattice parameter (2.9−4.1%) for Pd, whereas PdAu only marginally expands (0.4%) upon interaction with molecular H_2. Changes in the partial pressure of H_2 result in differences in the formation of PdH_α and/or PdH_β. At a partial pressure of 0.1 bar, both the α and β phases coexist in the 20 nm Pd film. The extreme sensitivity of the *in situ* GIXRD approach allows to monitor the transition from $Pd_{(metallic)} \rightarrow PdH_\alpha \rightarrow PdH_\beta$, its reversibility, and the stability of the films upon cycles of H_2. Exposure to C_2H_2 alone or mixtures of C_2H_2:H_2 at elevated temperatures results in the irreversible expansion of the Pd unit cell (2.5−3.5%), demonstrating the formation of a PdC_x interstitial solution (with homogeneous composition along the thickness of Pd), which hinders almost completely later hydride formation. PdAu forms an interstitial solution with C, although to a much lesser extent than that of the Pd films. The current work generates fundamental knowledge using thin-film catalysts, which represent a step between model and industrial systems. Our experiments close the pressure gap compared to previous experiments performed with ideal surfaces at very low pressures and allow to monitor the competitive dynamics of PdH_x and PdC_x formation in the catalytic subsurface.

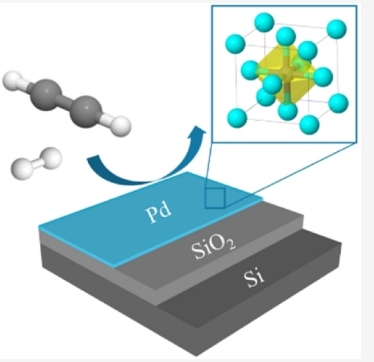

1. INTRODUCTION

Ethylene is a key chemical compound in the synthesis of surfactants, detergents, and plastics, among others. It is produced via the cracking of oil fractions or via the stepwise conversion of methane to acetylene to ethylene.[1] In both routes, significant amounts of unconverted acetylene remain, and their removal is mandatory to prevent poisoning of the ethylene polymerization catalyst.[2] The key performance indicator of this industrially applied reaction is the selectivity toward ethylene (eq 1); preventing overhydrogenation to ethane is of utmost importance (eq 2).

$$C_2H_2 + H_2 \leftrightarrow C_2H_4 \qquad \Delta H^\circ_{298\,K} = -176\ kJ{\cdot}mol^{-1} \quad (1)$$

$$C_2H_4 + H_2 \leftrightarrow C_2H_6 \qquad \Delta H^\circ_{298\,K} = -136\ kJ{\cdot}mol^{-1} \quad (2)$$

The performance of the catalyst is determined by three factors, often interrelated,[3] which have been tackled to fundamentally understand and optimize the catalytic process: First, the geometric effect, via, *e.g.*, site isolation,[4] change of the particle size,[5,6] and tuning of the exposed facet,[6,7] among others. Second, modification of the electronic effect has been achieved via the synthesis of substitutional alloys like PdAg[8] or PdAu[4,9] and intermetallic compounds[10] like Pd_2Ga,[3] Pd_3Ga_7,[11] and PdGa.[11] The improved selectivity of $PdAu_x$ catalysts has been associated with the isolation of Pd atoms,[4] tuning the binding energy of the reactants and the reaction kinetics:[12] little experimental evidence has been gathered regarding the subsurface chemistry of these alloys. Alloying of Pd with Au shifts the density of states (DOS) and as a consequence decreases the H_2 storage capacity.[13]

Third, the subsurface chemistry of the catalyst: the fundamental understanding of the interactions of Pd with H, the formation of subsurface PdH_x species, and their effect on

Received: March 27, 2025
Revised: June 20, 2025
Accepted: July 2, 2025
Published: July 11, 2025

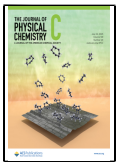

https://doi.org/10.1021/acs.jpcc.5c02040
J. Phys. Chem. C 2025, 129, 13312−13321

performance has been studied in depth,[6,7,14−17] spilling over to and nourishing other fields like membrane technology[18] and gas sensing.[19,20] Pd can dissociate molecular H_2, followed by the diffusion of H atoms into the bulk of the Pd and the occupation of the octahedral interstitials[2,13,21] to form solid solutions. As a function of the temperature and the partial pressure of H_2, two distinct phases can be formed at ambient conditions: the α (PdH_x, $x < 0.03$) and the β phases (PdH_x, $x > 0.03$).[13] In regard to catalysis, a higher concentration of H in the PdH_β phase results in a higher extent of overhydrogenation to ethane:[21] the intercalated H can diffuse to the surface and hydrogenate adsorbates,[22] a phenomenon of utmost importance for the reaction hereby studied. Numerous studies have shown that occupying the Pd interstitials with other species like C,[23] B,[24,25] or P[25] can mitigate the intercalation of H, decrease its subsurface concentration, and improve selectivity.[14,26,27] Similarly to PdH_x, PdC_x is reported to enhance the reaction rates compared to those of single Pd.[21] Surface carbon species can also modify the performance of the catalysts: thick graphitic multilayers tend to cover the active sites and hinder reaction rates,[2] whereas permeable carbon layers can isolate them and improve selectivity.[26,28] Another strategy to control the subsurface chemistry is based on tuning the size of the supported Pd nanoparticles, as smaller particles dissolve less H.[13,29] Carbon subsurface chemistry in nickel is also reported to play a critical role in the dry reforming of methane[30,31] and carbon nanofiber formation.[32]

Very recently, laterally condensed catalysts (LCCs) composed of very thin films of palladium deposited on flat substrates have been demonstrated for acetylene semihydrogenation.[33] This concept opens a new dimension in heterogeneous catalysis to link "fundamental studies" performed on model surfaces and the "applied approach" with industrial catalysts. On the one hand, model surfaces yield defined structures at conditions often far away from those of industrial relevance, suffering from the so-called pressure gap; on the other hand, the "applied approach" evaluates realistic structures that are too complex to be fully resolved and isolates the contribution of individual active sites, suffering from the material gap. The applied methodology differs significantly between model and real systems: *in situ* scattering experiments can be performed at realistic reaction conditions,[34,35] thanks to the diminished attenuation of the used X-rays compared to that of low(er)-energy X-rays generally used in spectroscopy. In any case, establishing structure−activity correlations, a key factor in catalytic research, remains complex. Deposition of catalytic thin films can also be applied to catalytic membrane reactors, opening exciting pathways for process intensification.[36,37] Furthermore, catalytic thin films enable to engineer alternative ways to supply the heat of reaction in more localized ways, *e.g.*, by induction heating.[38]

In this work, we build upon the recently introduced catalytic thin film concept[33] and the specifically designed synchrotron *in situ* grazing-incidence X-ray diffraction (GIXRD) cell[39] to study the dynamics of palladium and palladium−gold films upon PdH_x and PdC_x formation under realistic reaction conditions. We combine the *in situ* data with *ex situ* X-ray photoelectron spectroscopy (XPS) and transmission electron microscopy (TEM) to further expand the knowledge of the catalyst's subsurface dynamics, PdC_x and PdH_x competitive formation, and their stability.

2. EXPERIMENTAL METHODS

2.1. Catalyst Preparation: Thin Film Deposition. The $Pd/SiO_2/Si$ and $PdAu/SiO_2/Si$ samples were prepared by using thin-film deposition technologies. The starting support material were Silicon 6-in. wafers with (100) orientation from Siegert Wafer (Germany). These were initially prescribed using UV laser scribing (Keyence, 355 nm, 10 W, 40 kHz) to define the desired sample sizes for further analysis after deposition (9 × 9 or 10 × 10 mm^2). After the scribing process, the samples were cleaned using an ozone solution to remove organic contaminants (20 ppm of O_3 in DI water for 2 min) followed by drying in an oven at 75 °C for 12 min. Afterward, the samples were dipped in 1% HF (v/v) for 5 min to remove the native SiO_2 layer. A layer of SiO_2 (the goal of such layer is to prevent the Pd and Si to directly interact and avoid the formation of $PdSi_x$)[33] was deposited on top of the cleaned Si wafer with PECVD (plasma-enhanced chemical vapor deposition) using a CS400PS PECVD/PVD cluster tool from Von Ardenne (Germany). Initially, the samples were preheated for 5 min at 450 °C with a flow of 50 mL(STP)·min^{-1} of H_2 and 1 mbar chamber pressure. The deposition was performed at 450 °C, 0.3 mbar of pressure, 30 W RF power at a frequency of 60 MHz and 17 mm electrode distance for 18 s, with a gas mixture of SiH_4 (4 mL·min^{-1}, 5 N from Air Liquide) and N_2O (mL·min^{-1}, 5 N, from Air Liquide). Afterward, the samples were transferred into a magnetron sputter system (PREVAC) under a N_2 atmosphere. This controlled environment prevents oxidation or contamination during the transfer process. The deposition of Pd and PdAu thin films was performed at room temperature using magnetron sputtering. Pd and PdAu thin films were deposited using a 3N5 2-in. Pd target and a 4N 2-in. Au target. Argon flow rate of 1.8 mL·min^{-1} during the deposition, sputter pressure of $4{\cdot}10^{-3}$ mbar and a 13.56 MHz RF plasma operated at 50 W. Along this manuscript, the samples will be referred to as 3 nm Pd, 20 nm Pd, or 3 nm PdAu, with all of these thin films being supported on the same 20 nm SiO_2/Si substrate stack.

2.2. Catalyst Characterization. *In situ* grazing-incidence X-ray diffraction (GIXRD) (or grazing-incidence wide-angle X-ray scattering/GIWAXS) was performed at the μ-Spot beamline[40,41] of the BESSY-II synchrotron in Berlin, Germany, using a custom cell developed by our group.[39] The cell is composed of a CNC-milled body of brass, which was electroplated with gold to maximize inertness. The cell allows one to assemble square samples. A K-type thermocouple below the sample and inside the brass body (not in contact with the gas phase) allows us to measure the temperature and serves for temperature control, performed with a PID controller Model 336 from Lake Shore Cryotronics Inc. and powered by heating cartridges. An aluminum lid with a DuPont Kapton (polymide, 50 μm thick) window encloses the sample, forming a 1.3 mm wide space for gas flow from the inlet, on top of the sample's surface, and to the outlet of the reaction chamber. The small volume of gas above the sample allowed for swift changes of gas composition. An external dome encloses the first lid: this dome volume is at pressures slightly below atmospheric and works as a safety mechanism to prevent release of gases into the hutch in the case of leakage. The dome is made of aluminum with in and out windows for the X-rays made of Kapton. The gas flow of Ar, C_2H_2, and H_2 was controlled using three mass flow controllers (MFCs, El-Flow Prestige series, Bronkhorst). The volumetric flow per unit area of catalyst

https://doi.org/10.1021/acs.jpcc.5c02040
J. Phys. Chem. C 2025, 129, 13312−13321

($mL \cdot min^{-1} \cdot mm^{-2}$) was kept constant between the catalytic tests[33] and the *in situ* tests. A back pressure controller (El-Press, Bronkhorst) regulates the pressure inside the cell (always at 1.01 bar to 1 atm), and a compressor controls the pressure inside the dome, maintained at 0.8 bar. A mass spectrometer (Prisma 80, Pfeiffer Vacuum, Germany) allows for qualitative detection of the outlet gas composition. Diffraction measurements were performed at 17 keV incident photon energy (equivalent wavelength of 0.7293 Å) and a spot size (diameter) of 30 μm. The 2D detector employed is a Dectris Eiger 9 M, placed at a distance of about 300 mm from the sample. To calibrate the sample−detector distance (SDD), two different samples were used. First, a LaB_6 NIST 660b standard sample was prepared by spin-coating a suspension containing the standard on Si wafers (same size as the samples). Second, a sputtered pure Au thin film sample was deposited on a Si wafer using the same methodology as the Pd samples. For each incident angle (ω), calibration was done to account for the shift of the center of analysis (and consequently the SDD). This effect is more pronounced at very shallow angles. Upon heating, the cell expands, moving the sample from the calibrated position: to compensate for this factor, the height and tilt at each temperature were corrected using the reported methodology.[42] Tilt angles are between 0.1° and 0.3°. These result in different attenuation lengths, *i.e.*, different depths, are sampled at different angles, with the shallower angles being the most surface sensitive:[43] calculations are shown in Figure S1. The identified patterns in this work belong to Pd (PDF 00-046-1043, a= 3.890 Å), $PdH_{0.64}$ (PDF 00-084-0300, a= 4.03 Å), $PdH_{0.706}$ (PDF 00-018-0951, a= 4.02 Å), and PdAu (PDF 96-151-0275, a= 3.98 Å). Different experiments were performed: "Full experiment" (conditions in Figure S2, mimicking those performed in ref 33, correcting for the sample area to maintain the volumetric flow per area), "PdC_x formation" (conditions in Figure S3), "H_2-cycling" (conditions in Figure S4), and "H_2-partial pressure" (conditions in Figure S5).

The 2D detector images were processed using the DAWN software.[44,45] Using the calibration, the detector data (.h5 files) were transformed, masked (to remove artifacts, detector gaps, and "burned pixels") and azimuthally integrated. The resulting patterns were background-subtracted, normalized to the intensity of the (111) reflection, and exported for further processing. Reflections were fitted by using a Pseudo-Voigt function. The lattice parameters were calculated using the definition of the scattering vector q (eq 3) and the relationship between interplanar distance d and the Miller indices for cubic crystal systems (eq 4). The data set was further processed and plotted using Origin.[46] The standard deviation of the lattice parameters expressed in this work is ±0.01 Å.

$$d = \frac{2\pi}{q} \tag{3}$$

$$d = \frac{a}{\sqrt{h^2 + k^2 + l^2}} \tag{4}$$

X-ray photoelectron spectroscopy (XPS) measurements were conducted using nonmonochromatized Mg K_α (1253.56 eV) irradiation from a SPECS XR 50 X-ray source (Germany) at the Energy Materials *In-Situ* Laboratory Berlin (EMIL).[47] The photoelectrons were detected using a Scienta Argus CU electron analyzer (Sweden). The pass energy for the core-level detail spectra measurements was set to 20 eV, resulting in a total experimental energy resolution of approximately 1.0 ± 0.3 eV. The references for qualitatively discussing the spectra are shown in Table S1.

Samples for investigation in a transmission electron microscope (TEM) were prepared by using a Zeiss Crossbeam 340 Focused Ion Beam (FIB) for standard sample lift-out preparation. All samples were covered with protective carbon or platinum layers prior to starting the lift-out preparation itself. Observations by TEM were carried out in a Zeiss Libra 200FE TEM operated at 200 keV electron energy. The microscope is equipped with an in-column energy filter, which was used to obtain zero-loss filtered images with enhanced contrast. The Fiji software[48] was used for further processing of the images, including quantification of the layer thickness (average of at least 5 measurements).

3. RESULTS AND DISCUSSION

Figure 1 shows the lattice parameter of the Pd catalysts as a function of the reaction step obtained using *in situ* GIXRD

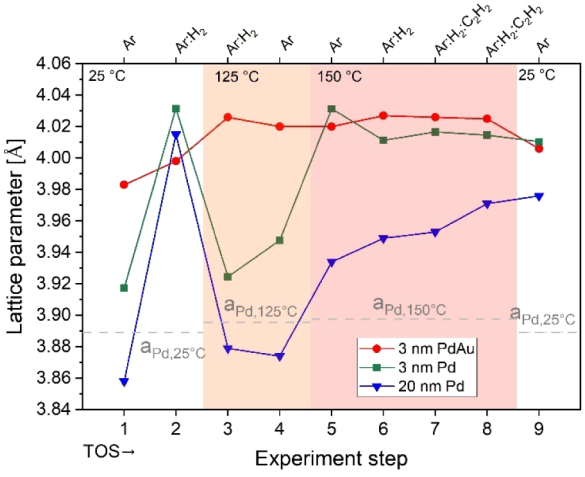

Figure 1. Lattice parameter as a function of the experiment step (increasing time on stream, TOS) obtained with *in situ* GIXRD following the "Full experiment". The detailed conditions are depicted in Figure S2. The reference a_{Pd} belongs to PDF 00-046-1043, and its value at higher temperature is calculated assuming isotropic thermal expansion.

during the "full experiment," which mimicked the catalytic test previously reported,[33] with the addition of a step with Ar:H_2 prior to the reaction mixture (Ar:H_2:C_2H_2) to monitor H-induced lattice expansion at 150 °C (step 6 in Figure 1). All samples maintained their $Fm\bar{3}m$ (PDF 00-046-1043) structure all along the experiment, albeit showing changes in the unit cell volume. No reflections of $PdSi_x$ can be observed, supporting the claim that a SiO_2 interlayer with a thickness of 20 nm or more prevents the diffusion of metals[33] (see Methods). The initial lattice parameter at room temperature differs slightly between the 3 and 20 nm Pd samples, probably caused by strain. The lattice parameter of the PdAu sample is higher than that of the pure Pd films, caused by the substitution of Au (atomic metal radii of 144 pm)[49] in the lattice of the $Fm\bar{3}m$ Pd structure (137 pm):[49] it can be better fitted to a $Fm\bar{3}m$ AuPd (PDF 96-151-0275) with a lattice parameter of 3.980 Å, while pure Au (PDF 96-110-0139) has a cubic lattice parameter of 4.070 Å.

https://doi.org/10.1021/acs.jpcc.5c02040
J. Phys. Chem. C 2025, 129, 13312−13321

The initial hydrogenation step (Figure 1, step 2) results in the expansion of the unit cell caused by the intercalation of H atoms in the interstitials of the Pd and PdAu films, forming hydrides (see Note S1 for the explanation of terminology). The extent is dependent on the layer, with the largest expansion of 4.1% being observed for the 20 nm Pd film, 2.9% for the 3 nm Pd film, and just 0.4% in the case of the PdAu film. The reduced storage capacity of H in the subsurface of $PdAuH_x$ could help to explain the more selective catalytic performance of the alloy reported previously,[4] together with the concept of site isolation. Upon heating under Ar:H_2 up to 125 °C, the lattice parameter of both Pd samples decreases: this is caused by a decrease in the concentration of H in the Pd:H system with increasing temperature.[13,50] Upon removal of the hydrogen gas at 125 °C, the lattice parameters remained rather unaltered. Subsequently, the sample is heated to 150 °C and initially exposed to an Ar:H_2 mixture, which results in a minimal change of the lattice parameter. Upon exposure to the reaction mixture (Figure 1, steps 7 and 8, both steps separated ∼120 min in time), the lattice parameter of Pd marginally changes, slightly increasing for the 20 nm Pd sample. The very minor changes in the lattice parameter observed during the reaction do not allow us to elucidate the formation of any PdH_x or PdC_x structures. Throughout the experiment, product distribution was tracked qualitatively with MS and demonstrated ethylene and ethane formation during the reaction step (Figure S6). Structural changes at the elevated temperature cannot be disregarded: these might result in small variations of the lattice parameter, which could mask minor effects occurring upon H and or C interstitial dissolution. At 150 °C, the Pd and PdAu unit cell remains expanded compared to pure thermal expansion. The last data point (9) displays the lattice parameter of the films at room temperature and after cooling under Ar atmosphere. The lack of H_2 in the gas phase results in desorption of H from the PdH_x film (see Figure 3): thus, none or a minimal amount of H in the subsurface of the Pd thin layer is expected in step 9 of Figure 1. Still, the different lattice parameters remain significantly expanded compared to the initial values: 4.006 Å (2.4% expansion) for the 3 nm Pd, 3.976 Å (3.0% expansion) for the 20 nm Pd, and 4.006 Å (0.6% expansion) for the PdAu sample. Such changes might be a result of the formation of a PdC_x system.[23] Carbon can occupy the same interstices as H, mitigating its subsurface concentration and influencing the selectivity of the target reaction.[14] Interestingly, intercalation of C in a PdAu catalyst for the vapor-phase vinyl acetate synthesis under different conditions, as hereby reported, was disregarded.[9] Disentanglement of PdH_x and PdC_x exclusively using XRD is not possible[51] unless a very careful design of the experiment is done (see Figure 2).

To reveal the existence of a PdC_x system and its competition with the formation of PdH_x, an *in situ* experiment was performed: heating up to the reaction temperature under Ar, exposure to Ar:C_2H_2 gas, cooling to room temperature, and final exposure to Ar:H_2 (see full conditions in Figure S3) while monitoring the crystal structure. Panel A of Figure 2 shows the significant increase in the lattice parameter of Pd upon heating to 150 °C and interaction with C_2H_2 gas. The values of the lattice parameter are above those of Pd at 150 °C (thermal expansion). This phenomenon is due to the occupation of the octahedral interstitials by C.[2,23,52] The 3 nm Pd layer (Figure 2B) already displays a fully expanded unit cell prior to the exposure to C_2H_2: the carbon present before the reaction (*i.e.*, contamination during or after deposition) fully occupies the interstitials. Indeed, both fresh samples contain similar amounts of carbon before exposure to the reactants, as revealed by XPS (see Figure 2C).

After 1 h under Ar:C_2H_2 flow and upon cooling to room temperature, the original cell volume is not recovered (as in Figure 1), remaining expanded. At this moment, a depth-resolved analysis was performed with the 20 nm Pd sample (data shown in Figure S7): the PdC_x lattice parameter remains constant along the thickness of the layer (a = 4.004 ± 0.005 Å, expansion of 3.4%), *i.e.*, no concentration gradient of C in the Pd film can be elucidated from GIXRD. This lattice parameter and expansion are higher than those previously reported[23,51,53] and point out to a supersaturated solid solution of C inside Pd. The 3 nm PdC_x shows a lattice parameter of 4.017 Å (expansion of 2.5%) at room temperature. After PdC_x formation, a hydrogenation step was done at the same conditions as those performed in Figure 1. Interestingly, the position of the reflections only marginally changes, resulting in an expansion of the lattice parameter by 0.2% (compared to the previous pattern). This observation highlights the lack of significant intercalation of H inside the PdC_x host, proving the formation of a PdC_x system: in other words, the occupation of the interstitials by C hinders the intercalation of H, minimizing the concentration of subsurface H.

In order to complement these insights with surface-sensitive information, the samples were recovered and analyzed with XPS postreaction. Figure S8 shows the XPS survey spectra of the Pd samples before (fresh) and after (spent) catalysis. According to the significant C 1s line at 285 eV binding energy, a significant amount of C can be found in/on the samples prior to the experiment, which we presumably attribute to C incorporated in the Pd during deposition or surface contamination upon air exposure of the samples. After the experiment, the total amount of C increases considerably, in particular, for the 20 nm Pd sample. For the latter, we also find a significant increase of the level of the binding energy of the O 1s signal at 530 eV, indicating the presence of a pronounced O- and C-containing layer on the sample surface (presumably as a result of additional surface contamination and/or coking during the GIXRD study), attenuating almost completely the Pd-related signals (most prominently the Pd 3d at 335 eV binding energy).

For the fresh 3 nm Pd sample, small Si 2p (at 100 eV binding energy) and Si 2s (at 150 eV binding energy) related signals can be observed in the XPS survey spectrum, indicating the very thin nature of the film. Note that the inelastic mean free path of the Si 2p photoelectrons in Pd is approximately 1.5 nm (calculated using QUASES-IMFP-TPP2M ver. 3.0, based on ref [54,55]), which allows XPS to probe the SiO_2/Si substrate stack through a 3 nm thick Pd film. The possibility of the film not being pinhole free was excluded based on the TEM results discussed below. After catalysis, the intensity of the Si-related peaks for the spent 3 nm Pd sample significantly decreases (and almost disappears), caused by the additional accumulation of C on the sample surface as indicated by the increased C 1s line and the related more pronounced attenuation of the substrate signals.

In order to check whether XPS also provides corroborating evidence for the formation of a Pd:C interstitial system, the Pd 3d detailed spectra (see Figure 2C.2) are closely inspected next. The Pd 3d line of the fresh 3 and 20 nm Pd samples are very similar, exhibiting an asymmetric peak shape (especially

https://doi.org/10.1021/acs.jpcc.5c02040
J. Phys. Chem. C 2025, 129, 13312−13321

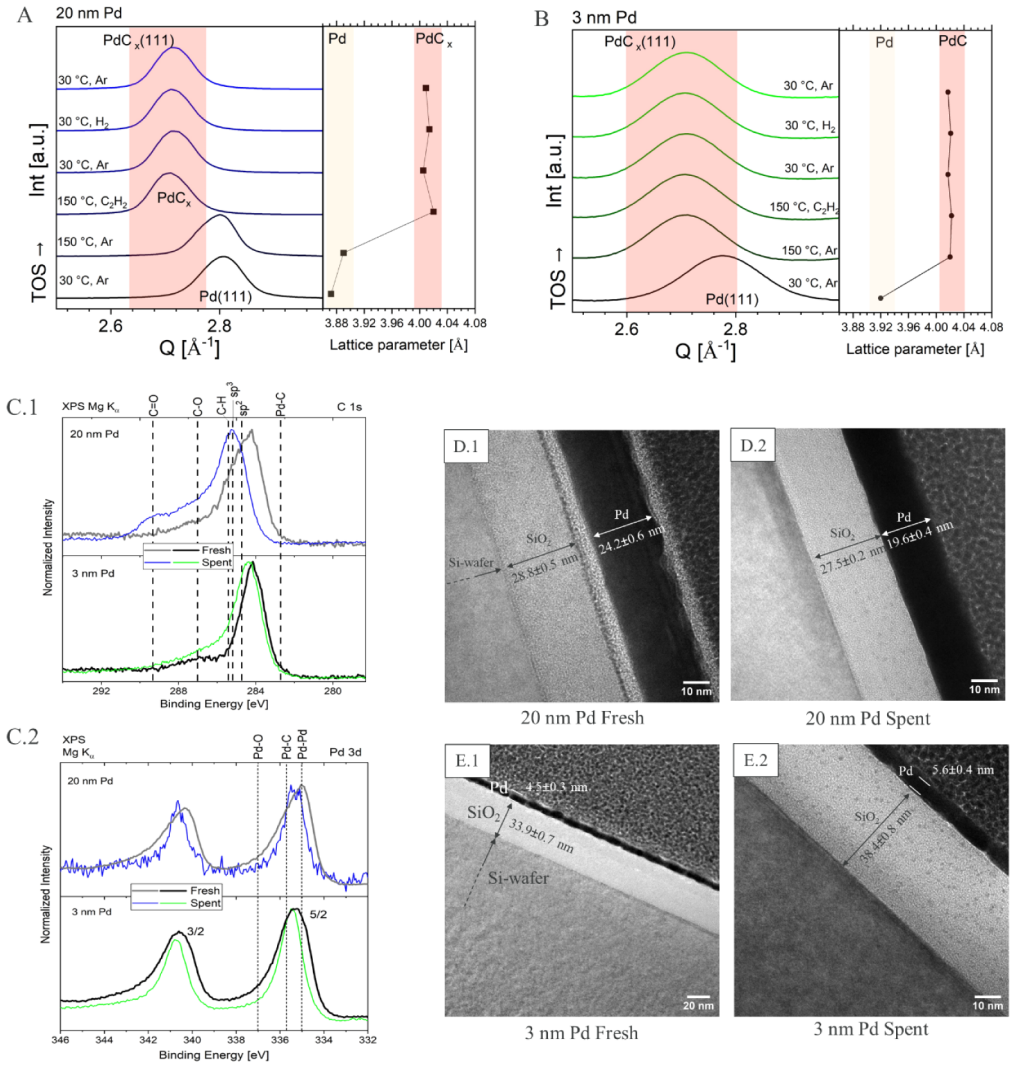

Figure 2. *In situ* GIXRD of the "PdC$_x$ formation" experiment (for details see Figure S3) for the (A) 20 nm Pd and (B) 3 nm Pd sample (red regions in the graph indicate PdC$_x$ whereas clear brown regions indicate Pd); (C.1) C 1s and (C.2) Pd 3d *ex situ* XPS spectra of the fresh and spent 3 nm Pd and 20 nm Pd samples (*i.e.*, before and after the "PdC$_x$ formation" GIXRD experiment). The most prominent photoemission lines in the survey spectra are labeled (see Table S1 for reference); TEM cross section images of lamella of the fresh and spent (D) 20 nm and (E) 3 nm Pd samples.

for the 20 nm Pd sample), indicating that Pd is mainly present in its metallic form. This is corroborated by the center of mass of the Pd 3d$_{5/2}$ lines being very close to the binding energy of Pd−Pd bonds of metallic Pd reported in the literature,[26] as indicated by the corresponding vertical dashed line in Figure 2C.2. The small deviation of the spectral shape (more symmetric) and the (higher) binding energy position of the Pd 3d line of the 3 nm (compared to that of the 20 nm) Pd sample is indicative of a significant presence of at least one additional Pd species, which could be related to the close proximity of the SiO$_2$/Si substrate. However, for the spent Pd samples, we find the Pd 3d spectral shape to become more symmetric, significantly narrower, and the peak position to be shifted to higher binding energies, independent of Pd thickness; all of which are in agreement with the GIXRD results indicating the formation of a PdC$_x$ system upon exposure to catalytic conditions (see Note S2 for more details on the XPS analysis). Note that the Pd 3d spectrum of the spent 20 nm Pd sample has a significantly lower signal-to-noise ratio due to the pronounced attenuation of the signal caused by the pronounced O- and C-containing surface layer discussed above. Analysis of the XPS C 1s spectra shown in Figure 2C.1 leads to unclear results and did not unequivocally allow us to identify a PdC$_x$ signal (see Note S2 for a full explanation).

Figure 2D,E displays the cross-section TEM studies of the lamellar fresh and spent 3 and 20 nm samples. The thin films appear closed after deposition, with a mild delamination occurring in the fresh 20 nm sample. The PdC$_x$ spent samples appeared unaltered, highlighting the stability of the materials during the experiment. As a conclusion, the "PdC$_x$ formation" experiment proves the formation of an intercalated PdC$_x$ compound that almost completely hinders the later PdH$_x$ formation. C was already present in the films before exposure to C$_2$H$_2$ and increases significantly on the surface of the Pd films after the reaction, without structural damage. This carbon would not prevent hydride formation until the samples are heated and, for the 20 nm sample, exposed to acetylene; therefore, the carbon was not occupying the interstitials until

https://doi.org/10.1021/acs.jpcc.5c02040
J. Phys. Chem. C 2025, 129, 13312−13321

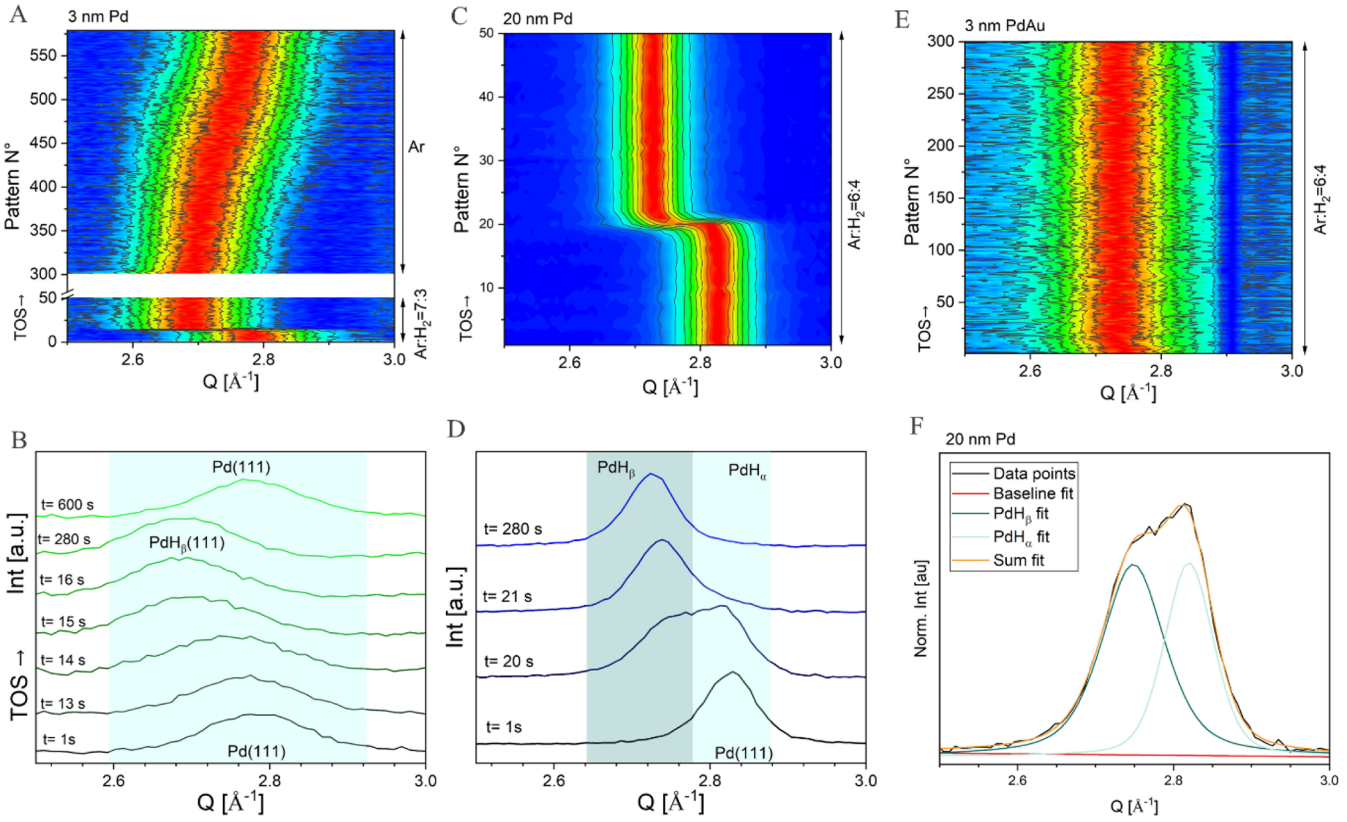

Figure 3. *In situ* GIXRD data showing contour maps (top) and selected patterns (bottom) of the 3 nm Pd (panel A and B), 20 nm Pd (panel C and D), and 3 nm PdAu (panel E) exposed at RT to Ar:H_2 (6:4 or 7:3 see right part of each graph) and subsequent Ar flows. Each pattern translates to an ∼1 s acquisition time and has been normalized. The selected patterns in panels B and D are stacked. Panel F shows the deconvolution of the pattern obtained at t = 20 s in panel D.

reaction conditions, allowing for hydride formation. After exposure to acetylene, the C content increases.

Thus, it becomes evident that PdC_x hinders the formation of PdH_x: this is reported to have an impact on the catalytic performance.[14,33] Still, the intercalation of H inside the Pd before the reaction is of fundamental interest and is hereby further explored. Figure 3 shows the time-resolved *in situ* GIXRD data of the hydrogenation step (Ar:H_2= 6:4 for the 20 nm Pd and 3 nm PdAu samples, Ar:H_2 = 7:3 for the 3 nm Pd sample) at room temperature. For the 3 and 20 nm Pd films, exposure to Ar:H_2 flow results in the fast shift (few seconds) of the Pd (111) reflection to lower values of the scattering vector, while this expansion is minimal for the PdAu sample (Figure 3E). Upon removal of H_2 from the gas phase, the reflections begin to shift back to their original position, much slower compared to the intercalation process (see Figure 3A), as previously reported.[56,57] The reason is that the rate-determining step for the decomposition of PdH_x is the slow associative desorption from the metal−gas interface. There is an increase in the fwhm during this process, probably caused by the coexistence of regions with slightly different concentrations of interstitial H. The formation of Pd:H systems depends to some degree on the layer's thickness. On the one hand, the 20 nm Pd sample proceeds via the coexistence of two transient clearly differentiated phases of PdH_x for a very short span of time (around 1 s). The obtained pattern at 20 s is deconvoluted in Figure 3F into two pseudo-Voigt fit functions, which yield lattice parameters of 3.859 and 3.960 Å, expanded 0.2% and 2.8% compared to the initial lattice parameter of 3.852 Å (time = 0 s); these can be attributed to PdH_α and PdH_β, respectively. At the end of the experiment, the last pattern yields a lattice parameter of 3.994 Å (expansion of 3.7% compared to the initial). The lattice values of the PdH_β are close to $PdH_{0.64}$ (PDF 00-084-0300, $Fm\bar{3}m$, a = 4.03 Å) or $PdH_{0.706}$ (PDF 00-018-0951, $Fm\bar{3}m$, a = 4.02 Å). On the other hand, hydride formation on the 3 nm Pd seems to proceed via the existence of a single compound, which reaches a final PdH_β with lattice parameter of 4.050 Å (3.6% expansion). We cannot disregard that different phases coexisted in the thin sample although they are not observed, which could be caused by the very short acquisition times and the little amount of scattering material. The same reasons yield rather noisy patterns for this and the PdAu films. For the 3 nm thin films, the fwhm of the reflections is broader compared to that of the 20 nm film; this clearly indicates a smaller crystallite size, which certainly occupies the full layer thickness.

From this experiment, it is not clear whether the original lattice parameter is recovered after dehydrogenation. To shed further light on this phenomenon's reversibility and the stability of Pd films upon cycles of H-sorption and desorption, the results of H_2 cycling on a 3 nm Pd sample are shown in Figure S9 (conditions in Figure S4). The initial lattice parameter of 3.911 Å expands to 4.050 Å upon H-intercalation without variance for the first two cycles (3.6% expansion). After 10 cycles, the lattice parameter of the PdH_β phase remains fairly constant at 4.060 Å. Upon removal of H_2 from the gas phase, the exsolution process is not complete, remaining relatively expanded at 3.971 Å (1.5%). Other

https://doi.org/10.1021/acs.jpcc.5c02040
J. Phys. Chem. C 2025, 129, 13312−13321

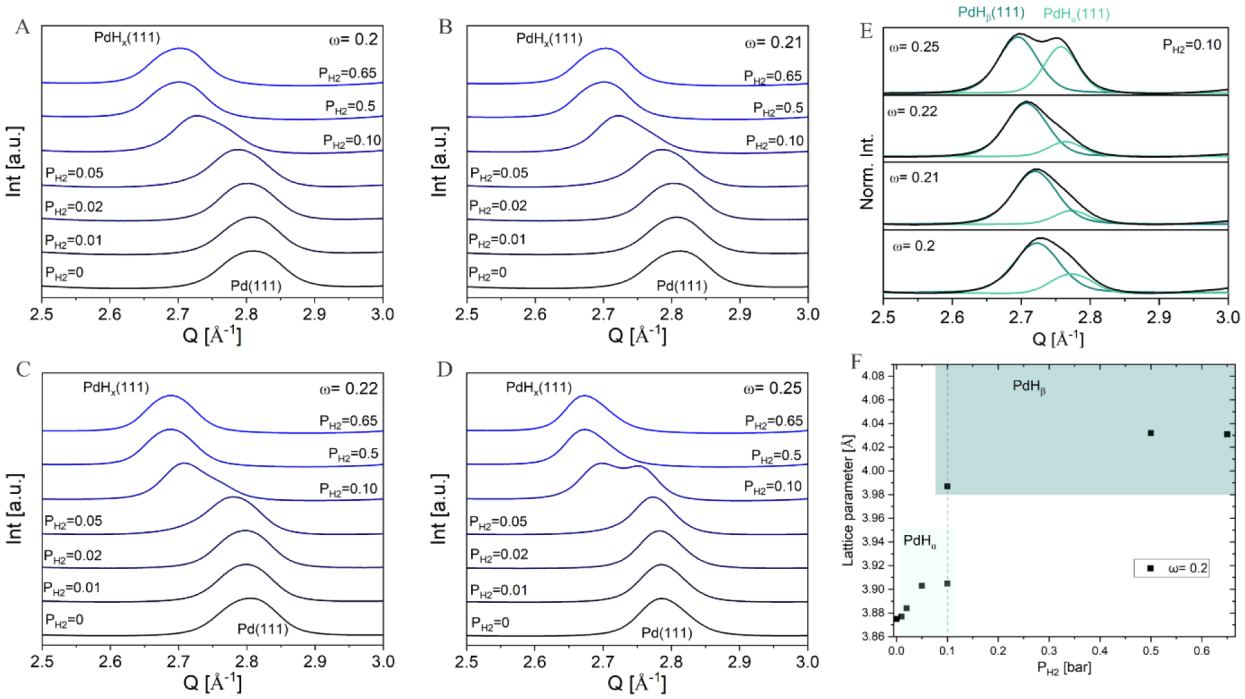

Figure 4. Depth-resolved PdH_x formation at different P_{H2} on a 20 nm Pd film, as revealed using *in situ* GIXRD: all experiments are performed at different Ar:H_2 ratios but at constant p = 1 atm (a) and volumetric flow per area of 0.6239 mL·min^{-1}·mm^{-2} (full conditions in Figure S5). Panel E: depth-resolved PdH_x(111) and deconvolution to PdH_α and PdH_β for different incident angles (ω) at P_{H2} = 0.1 atm. Panel F: lattice parameter of the PdH_x as a function of the P_{H2} at ω = 0.2.

studies[52,56,58] have documented the loss of reversible H-sorption capacity during cycles of H insertion and removal or the change in the sorption/desorption kinetics.[57] Figure S9B shows the TEM lamellar cross sections before and after the cycles. The layer partially suffers dewetting: particle agglomeration occurs, highlighted by the appearance of discontinuities and the increase of the layer thickness and the standard deviation. H_2 cycling is reported to cause cracks and delamination,[59] although such inconvenient behavior shall be suppressed in films thinner than 20 nm.[60]

The content of H in the PdH_α phase (*i.e.*, the degree of occupation of the interstitials by H) is a function of the partial pressure of H_2 in the gas phase.[13] To quantify the existence of α and β phases and the expansion of the host's unit cell, a 20 nm Pd thin film has been monitored using GIXRD at different partial pressures of H_2 and incident angles (*i.e.*, at different attenuation lengths). In Figure 4A–D, the maxima of the reflection progressively shift toward lower values of the scattering vector upon increasing the partial pressure of H_2. At P_{H2}= 0.1 atm, the asymmetric broadening of the reflection concomitant with a shift to lower values occurs, pointing to the coexistence of more than one phase of PdH, *i.e.*, PdH_α and PdH_β. A depth-resolved analysis was performed at P_{H2}= 0.1 atm (Figure 4E): by increasing the incidence angle, the PdH_α/PdH_β ratio does not change, except for the ω = 0.25 (attenuation length of 71.60 nm). This could be due to lattice distortion at the Pd–SiO_2 interface. Above P_{H2} = 0.5 atm, a single PdH_β phase is observed. The obtained lattice parameters of this experiment at ω = 0.2 are shown in Figure 4F and show an increase from the original 3.876 Å with increasing P_{H2}. At P_{H2} > 0.5 atm, the lattice parameter of the β-phase remains constant at 4.031 Å (expansion of 4.0%).

4. CONCLUSIONS

The current work presents the first *in situ* observations of the dynamics of catalytic thin films under realistic operation conditions. We generate fundamental knowledge using thin-film catalysts, an emerging concept in the field of heterogeneous catalysis, whose material complexity lies between model and industrial systems. Our experiments close the pressure gap compared to previous experiments performed with ideal surfaces at very low pressures and allow us to monitor the competitive dynamics of PdH_x and PdC_x formation in the catalytic subsurface.

In situ GIXRD enables us to follow changes in the unit cell volume of Pd and PdAu catalytic thin films under mixtures of H_2 and C_2H_2 at temperatures relevant for acetylene semi-hydrogenation. PdH_x formation occurs at room temperature, with a significant increase in the lattice parameter for Pd, whereas PdAu marginally expands its unit cell upon interaction with molecular H_2. Both the 3 and 20 nm Pd thin films result in analogous PdH_x compounds (% unit cell expansion), displaying similar H_2 storage capacity. Changes in the partial pressure of H_2 at room temperature result in a different degree of occupation of the interstitial site, *i.e.*, in the formation of PdH_α and/or PdH_β. At a partial pressure of 0.1 bar, both α and β phases coexist in the 20 nm Pd film. The extreme sensitivity of our *in situ* tool allows to monitor the transition from $Pd_{(metallic)} \rightarrow PdH_\alpha \rightarrow PdH_\beta$, its reversibility, and the stability of the films upon cycles of H_2.

Exposure to C_2H_2 alone or mixtures of C_2H_2:H_2 at elevated temperatures results in the irreversible expansion of the Pd unit cell (2.5–3.5%), demonstrating the formation of a PdC_x interstitial solution, which hinders almost completely later hydride formation at room temperature. Our results suggest the formation of an interstitial solution of $PdAuC_x$, albeit to a

https://doi.org/10.1021/acs.jpcc.5c02040
J. Phys. Chem. C 2025, 129, 13312–13321

much lesser extent than the Pd films. Although already present prior to the interaction with C_2H_2, carbon contained in the fresh films would not hinder hydride formation until heated to the reaction temperature. The PdC_x resulting compound shows a constant lattice parameter along the thickness of the 20 nm Pd film.

■ ASSOCIATED CONTENT

Supporting Information

The Supporting Information is available free of charge at https://pubs.acs.org/doi/10.1021/acs.jpcc.5c02040.

Attenuation length through Pd (Figure S1); operating conditions of the "Full experiment" (Figure S2); operating conditions of the "PdC_x formation" (Figure S3); operating conditions of the "H_2 cycling" (Figure S4); operating conditions of the "H_2 partial pressure" (Figure S5); MS signal as a function of the time on stream (Figure S6); normalized intensity as function of Q (Figure S7); XPS survey spectrum of the 3 and 20 nm Pd samples (Figure S8); H_2-cycling experiment on a 3 nm Pd sample (Figure S9); reference binding energy positions for the qualitative evaluation of the XPS spectra (Table S1); clarification of terminology—use of the term "carbide" and "hydride" (Note S1); limitations of the XPS analysis for the identification of Pd:C (Note S2) (PDF)

■ AUTHOR INFORMATION

Corresponding Author

Albert Gili − *Helmholtz-Zentrum Berlin für Materialien und Energie, 14109 Berlin, Germany;* orcid.org/0000-0001-7944-7881; Email: albert.gili@helmholtz-berlin.de

Authors

Lukas Thum − *Helmholtz-Zentrum Berlin für Materialien und Energie, 14109 Berlin, Germany*

Meysam Khodabakhshi − *Helmholtz-Zentrum Berlin für Materialien und Energie, 14109 Berlin, Germany*

Shivam Shivam − *Helmholtz-Zentrum Berlin für Materialien und Energie, 14109 Berlin, Germany*

Raul Garcia-Diez − *Helmholtz-Zentrum Berlin für Materialien und Energie, 14109 Berlin, Germany;* orcid.org/0009-0000-9374-1083

Marcus Bär − *Helmholtz-Zentrum Berlin für Materialien und Energie, 14109 Berlin, Germany; Department of X-ray Spectroscopy at Interfaces of Thin Films, Helmholtz-Institute Erlangen-Nürnberg for Renewable Energy (HIERN), 12489 Berlin, Germany; Department of Chemistry and Pharmacy, Friedrich-Alexander-Universität Erlangen-Nürnberg (FAU), 91058 Erlangen, Germany;* orcid.org/0000-0001-8581-0691

Markus Wollgarten − *Helmholtz-Zentrum Berlin für Materialien und Energie, 14109 Berlin, Germany*

Rutger Schlatmann − *Helmholtz-Zentrum Berlin für Materialien und Energie, 14109 Berlin, Germany;* orcid.org/0000-0002-5951-9435

Daniel Amkreutz − *Helmholtz-Zentrum Berlin für Materialien und Energie, 14109 Berlin, Germany*

Complete contact information is available at: https://pubs.acs.org/10.1021/acs.jpcc.5c02040

Author Contributions

A.G.: conceptualization, methodology development, formal analysis, investigation, data curation, writing, visualization, project administration. L.T.: investigation, methodology development, writing—review and editing. M.K.: investigation, writing—review and editing. S.S.: investigation, writing—review and editing. R.G.D.: XPS investigation, data curation and evaluation, writing—review and editing. M.B.: supervision, funding acquisition, XPS data evaluation, writing—review and editing. M.W.: investigation, writing—review and editing. R.S.: supervision, funding acquisition, writing—review and editing. D.A.: supervision, writing—review and editing

Notes

The authors declare no competing financial interest.

■ ACKNOWLEDGMENTS

This work was funded by the German Federal Ministry of Education and Research in the framework of the project Catlab (03EW0015A). We appreciate the contribution of Martin Muske, Tobias Köhler, and Alex Steigert for sample preparation and of Johannes Frisch for supporting with the XPS measurements. The Energy Materials *In-situ* Laboratory Berlin (EMIL) is acknowledged for providing the infrastructure for Pd deposition and XPS measurements. We appreciate the work of the instrumentation department of BESSY-II: Dirk Wallacher and Nico Grimm. Finally, we very much thank Ivo Zizak for beamline support and his great expertise and Paulina Summa for her support in the beamline and for the insightful discussions.

■ REFERENCES

(1) Shittu, T. D.; Ayodele, O. B. Catalysis of semihydrogenation of acetylene to ethylene: current trends, challenges, and outlook. *Front. Chem. Sci. Eng.* **2022**, *16* (7), 1031−1059.

(2) Armbrüster, M.; Behrens, M.; Cinquini, F.; Föttinger, K.; Grin, Y.; Haghofer, A.; Klötzer, B.; Knop-Gericke, A.; Lorenz, H.; Ota, A.; et al. How to Control the Selectivity of Palladium-based Catalysts in Hydrogenation Reactions: The Role of Subsurface Chemistry. *ChemCatchem* **2012**, *4* (8), 1048−1063.

(3) Wowsnick, G.; Teschner, D.; Kasatkin, I.; Girgsdies, F.; Armbrüster, M.; Zhang, A.; Grin, Y.; Schlögl, R.; Behrens, M. Surface dynamics of the intermetallic catalyst Pd_2Ga, Part I − Structural stability in UHV and different gas atmospheres. *J. Catal.* **2014**, *309*, 209−220.

(4) Foucher, A. C.; Ngan, H. T.; Shirman, T.; Filie, A.; Duanmu, K.; Aizenberg, M.; Madix, R. J.; Friend, C. M.; Aizenberg, J.; Sautet, P.; Stach, E. A. Influence of Pd Concentration in Au−Pd Nanoparticles for the Hydrogenation of Alkynes. *ACS Appl. Nano Mater.* **2023**, *6* (24), 22927−22938.

(5) Tew, M. W.; Janousch, M.; Huthwelker, T.; van Bokhoven, J. A. The roles of carbide and hydride in oxide-supported palladium nanoparticles for alkyne hydrogenation. *J. Catal.* **2011**, *283* (1), 45−54.

(6) Crespo-Quesada, M.; Yoon, S.; Jin, M.; Prestianni, A.; Cortese, R.; Cárdenas-Lizana, F.; Duca, D.; Weidenkaff, A.; Kiwi-Minsker, L. Shape-Dependence of Pd Nanocrystal Carburization during Acetylene Hydrogenation. *J. Phys. Chem. C* **2015**, *119* (2), 1101−1107.

(7) Xu, Y.; Bian, W.; Pan, Q.; Chu, M.; Cao, M.; Li, Y.; Gong, Z.; Wang, R.; Cui, Y.; Lin, H.; et al. Revealing the Active Sites of Pd Nanocrystals for Propyne Semihydrogenation: From Theory to Experiment. *ACS Catal.* **2019**, *9* (9), 8471−8480.

(8) Han, Y.; Peng, D.; Xu, Z.; Wan, H.; Zheng, S.; Zhu, D. TiO_2 supported Pd@Ag as highly selective catalysts for hydrogenation of acetylene in excess ethylene. *Chem. Commun.* **2013**, *49* (75), 8350−8352.

(9) Han, Y.-F.; Kumar, D.; Sivadinarayana, C.; Clearfield, A.; Goodman, D. W. The Formation of PdC_x over Pd-Based Catalysts in Vapor-Phase Vinyl Acetate Synthesis: Does a Pd−Au Alloy Catalyst Resist Carbide Formation? *Catal. Lett.* **2004**, *94* (3/4), 131−134.
(10) Armbrüster, M.; Grin, Y. Intermetallic compounds in heterogeneous catalysis. *Sci. Technol. Adv. Mater.* **2020**, *21* (1), 767.
(11) Armbrüster, M.; Kovnir, K.; Behrens, M.; Teschner, D.; Grin, Y.; Schlögl, R. Pd-Ga intermetallic compounds as highly selective semihydrogenation catalysts. *J. Am. Chem. Soc.* **2010**, *132* (42), 14745−14747.
(12) Ngan, H. T.; Yan, G.; van der Hoeven, J. E. S.; Madix, R. J.; Friend, C. M.; Sautet, P. Hydrogen Dissociation Controls 1-Hexyne Selective Hydrogenation on Dilute Pd-in-Au Catalysts. *ACS Catal.* **2022**, *12* (21), 13321−13333.
(13) Dekura, S.; Kobayashi, H.; Kusada, K.; Kitagawa, H. Hydrogen in Palladium and Storage Properties of Related Nanomaterials: Size, Shape, Alloying, and Metal-Organic Framework Coating Effects. *ChemPhyschem* **2019**, *20* (10), 1158−1176.
(14) Teschner, D.; Borsodi, J.; Wootsch, A.; Révay, Z.; Hävecker, M.; Knop-Gericke, A.; Jackson, S. D.; Schlögl, R. The roles of subsurface carbon and hydrogen in palladium-catalyzed alkyne hydrogenation. *Science* **2008**, *320* (5872), 86−89.
(15) Bugaev, A. L.; Usoltsev, O. A.; Guda, A. A.; Lomachenko, K. A.; Pankin, I. A.; Rusalev, Y. V.; Emerich, H.; Groppo, E.; Pellegrini, R.; Soldatov, A. V.; et al. Palladium Carbide and Hydride Formation in the Bulk and at the Surface of Palladium Nanoparticles. *J. Phys. Chem. C* **2018**, *122* (22), 12029−12037.
(16) Velasco-Vélez, J. J.; Teschner, D.; Girgsdies, F.; Hävecker, M.; Streibel, V.; Willinger, M. G.; Cao, J.; Lamoth, M.; Frei, E.; Wang, R.; et al. The Role of Adsorbed and Subsurface Carbon Species for the Selective Alkyne Hydrogenation Over a Pd-Black Catalyst: An Operando Study of Bulk and Surface. *Top. Catal.* **2018**, *61* (20), 2052−2061.
(17) Teschner, D.; Vass, E.; Havecker, M.; Zafeiratos, S.; Schnorch, P.; Sauer, H.; Knopgericke, A.; Schlogl, R.; Chamam, M.; Wootsch, A. Alkyne hydrogenation over Pd catalysts: A new paradigm. *J. Catal.* **2006**, *242* (1), 26−37.
(18) Jokar, S. M.; Farokhnia, A.; Tavakolian, M.; Pejman, M.; Parvasi, P.; Javanmardi, J.; Zare, F.; Gonçalves, M. C.; Basile, A. The recent areas of applicability of palladium based membrane technologies for hydrogen production from methane and natural gas: A review. *Int. J. Hydrogen Energy* **2023**, *48* (16), 6451−6476.
(19) Li, Q.; Wang, L.; Xiao, A.; Zhu, L.; Yang, Z. Hydrogen sensing towards palladium-based nanocomposites: A review. *Int. J. Hydrogen Energy* **2025**, *136*, 1282.
(20) Gurlo, A.; Clarke, D. R. High-sensitivity hydrogen detection: hydrogen-induced swelling of multiple cracked palladium films on compliant substrates. *Angew. Chem., Int. Ed.* **2011**, *50* (43), 10130−10132.
(21) Borodziński, A.; Bond, G. C. Selective Hydrogenation of Ethyne in Ethene-Rich Streams on Palladium Catalysts. Part 1. Effect of Changes to the Catalyst During Reaction. *Catal. Rev.* **2006**, *48* (2), 91−144.
(22) Johnson, A. D.; Daley, S. P.; Utz, A. L.; Ceyer, S. T. The Chemistry of Bulk Hydrogen: Reaction of Hydrogen Embedded in Nickel with Adsorbed CH_3. *Science* **1992**, *257* (5067), 223−225.
(23) Stachurski, J.; Frąckiewicz, A. A new phase in the Pd-C system formed during the catalytic hydrogenation of acetylene. *J. less-Common Met.* **1985**, *108* (2), 249−256.
(24) Büchele, S.; Chen, Z.; Fako, E.; Krumeich, F.; Hauert, R.; Safonova, O. V.; López, N.; Mitchell, S.; Pérez-Ramírez, J. Carrier-Induced Modification of Palladium Nanoparticles on Porous Boron Nitride for Alkyne Semi-Hydrogenation. *Angew. Chem., Int. Ed.* **2020**, *132* (44), 19807−19812.
(25) Mousavi, S.; Keshavarz, M. H.; Moeini, S. Palladium doped with boron and phosphorus on activated carbon: a high-performance nanocatalyst for the hydrogenation of alkenes. *Mater. Today Chem.* **2023**, *28*, 101360.
(26) Liu, Y.; Fu, F.; McCue, A.; Jones, W.; Rao, D.; Feng, J.; He, Y.; Li, D. Adsorbate-Induced Structural Evolution of Pd Catalyst for Selective Hydrogenation of Acetylene. *ACS Catal.* **2020**, *10* (24), 15048−15059.
(27) Garcia-Ortiz, A.; Vidal, J. D.; Iborra, S.; Climent, M. J.; Cored, J.; Ruano, D.; Pérez-Dieste, V.; Concepción, P.; Corma, A. Synthesis of a hybrid Pd0/Pd-carbide/carbon catalyst material with high selectivity for hydrogenation reactions. *J. Catal.* **2020**, *389*, 706−713.
(28) Kim, H.; Robertson, A. W.; Kim, S. O.; Kim, J. M.; Warner, J. H. Resilient High Catalytic Performance of Platinum Nanocatalysts with Porous Graphene Envelope. *ACS Nano* **2015**, *9* (6), 5947−5957.
(29) Tew, M. W.; Miller, J. T.; van Bokhoven, J. A. Particle Size Effect of Hydride Formation and Surface Hydrogen Adsorption of Nanosized Palladium Catalysts: L_3 Edge vs K Edge X-ray Absorption Spectroscopy. *J. Phys. Chem. C* **2009**, *113* (34), 15140−15147.
(30) Gili, A.; Schlicker, L.; Bekheet, M.; Görke, O.; Kober, D.; Simon, U.; Littlewood, P.; Schomäcker, R.; Doran, A.; Gaissmaier, D.; et al. Revealing the Mechanism of Multiwalled Carbon Nanotube Growth on Supported Nickel Nanoparticles by In situ Synchrotron X-ray Diffraction, Density Functional Theory, and Molecular Dynamics Simulations. *ACS Catal.* **2019**, *9*, 6999−7011.
(31) Gili, A.; Schlicker, L.; Bekheet, M. F.; Görke, O.; Penner, S.; Grünbacher, M.; Götsch, T.; Littlewood, P.; Marks, T. J.; Stair, P. C.; et al. Surface Carbon as a Reactive Intermediate in Dry Reforming of Methane to Syngas on a 5% Ni/MnO Catalyst. *ACS Catal.* **2018**, *8*, 8739−8750.
(32) Gili, A.; Kunz, M.; Gaissmaier, D.; Jung, C.; Jacob, T.; Lunkenbein, T.; Hetaba, W.; Dembélé, K.; Selve, S.; Schomäcker, R.; et al. Discovery and Characterization of a Metastable Cubic Interstitial Nickel-Carbon System with an Expanded Lattice. *ACS Nano* **2025**, *19* (2), 2769−2776.
(33) Li, Z.; Öztuna, E.; Skorupska, K.; Vinogradova, O. V.; Jamshaid, A.; Steigert, A.; Rohner, C.; Dimitrakopoulou, M.; Prieto, M. J.; Kunkel, C.; et al. Rationally designed laterally-condensed-catalysts deliver robust activity and selectivity for ethylene production in acetylene hydrogenation. *Nat. Commun.* **2024**, *15* (1), 10660.
(34) Landers, A. T.; Peng, H.; Koshy, D. M.; Lee, S. H.; Feaster, J. T.; Lin, J. C.; Beeman, J. W.; Higgins, D.; Yano, J.; Drisdell, W. S.; et al. Dynamics and Hysteresis of Hydrogen Intercalation and Deintercalation in Palladium Electrodes: A Multimodal In Situ X-ray Diffraction, Coulometry, and Computational Study. *Chem. Mater.* **2021**, *33* (15), 5872−5884.
(35) Chattot, R.; Martens, I.; Mirolo, M.; Ronovsky, M.; Russello, F.; Isern, H.; Braesch, G.; Hornberger, E.; Strasser, P.; Sibert, E.; et al. Electrochemical Strain Dynamics in Noble Metal Nanocatalysts. *J. Am. Chem. Soc.* **2021**, *143* (41), 17068−17078.
(36) Habib, M. A.; Harale, A.; Paglieri, S.; Alrashed, F. S.; Al-Sayoud, A.; Rao, M. V.; Nemitallah, M. A.; Hossain, S.; Hussien, M.; Ali, A.; et al. Palladium-Alloy Membrane Reactors for Fuel Reforming and Hydrogen Production: A Review. *Energy Fuels* **2021**, *35* (7), 5558−5593.
(37) Ye, S.-Y.; Tanaka, S.; Esashi, M.; Hamakawa, S.; Hanaoka, T.; Mizukami, F. Thin palladium membrane microreactors with oxidized porous silicon support and their application. *J. Micromech. Microeng.* **2005**, *15* (11), 2011−2018.
(38) Wang, W.; Tuci, G.; Duong-Viet, C.; Liu, Y.; Rossin, A.; Luconi, L.; Nhut, J.-M.; Nguyen-Dinh, L.; Pham-Huu, C.; Giambastiani, G. Induction Heating: An Enabling Technology for the Heat Management in Catalytic Processes. *ACS Catal.* **2019**, *9* (9), 7921−7935.
(39) Thum, L.; Arztmann, M.; Zizak, I.; Grüneberger, R.; Steigert, A.; Grimm, N.; Wallacher, D.; Schlatmann, R.; Amkreutz, D.; Gili, A. In situ cell for grazing-incidence x-ray diffraction on thin films in thermal catalysis. *Rev. Sci. Instrum.* **2024**, *95* (3), 033904.
(40) Zizak, I. The mySpot beamline at BESSY II. *J. Large-Scale Res. Facil. JLSRF* **2016**, *2*, A102.
(41) Zizak, I. mySpot: a versatile microfocussing station for scanning methods at BESSY II. *J. Large-Scale Res. Facil. JLSRF* **2016**, *2*, A101.

https://doi.org/10.1021/acs.jpcc.5c02040
J. Phys. Chem. C 2025, 129, 13312−13321

(42) Harrington, G. F.; Santiso, J. Back-to-Basics tutorial: X-ray diffraction of thin films. *J Electroceram.* **2021**, *47* (4), 141−163.
(43) *Henke.lbl.gov.* https://henke.lbl.gov/optical_constants/atten2.html. accessed 17 January 2025.
(44) Filik, J.; Ashton, A. W.; Chang, P. C. Y.; Chater, P. A.; Day, S. J.; Drakopoulos, M.; Gerring, M. W.; Hart, M. L.; Magdysyuk, O. V.; Michalik, S.; et al. Processing two-dimensional X-ray diffraction and small-angle scattering data in DAWN 2. *J. Appl. Crystallogr.* **2017**, *50* (Pt 3), 959−966.
(45) Basham, M.; Filik, J.; Wharmby, M. T.; Chang, P. C. Y.; El Kassaby, B.; Gerring, M.; Aishima, J.; Levik, K.; Pulford, B. C. A.; Sikharulidze, I.; et al. Data Analysis WorkbeNch (DAWN). *J Synchrotron Rad.* **2015**, *22* (3), 853−858.
(46) Origin(Pro) *Version 2022b*; OriginLab Corporation: Northampton, MA, USA. https://www.originlab.com/index.aspx?go=Company&pid=1130.
(47) Hsieh, T.-E.; Frisch, J.; Wilks, R. G.; Papp, C.; Bär, M. Impact of Catalysis-Relevant Oxidation and Annealing Treatments on Nanostructured GaRh Alloys. *ACS Appl. Mater. Interfaces* **2024**, *16* (15), 19858−19865.
(48) Schindelin, J.; Arganda-Carreras, I.; Frise, E.; Kaynig, V.; Longair, M.; Pietzsch, T.; Preibisch, S.; Rueden, C.; Saalfeld, S.; Schmid, B.; et al. Fiji: an open-source platform for biological-image analysis. *Nat. Methods* **2012**, *9* (7), 676−682.
(49) Lide, D. R. *CRC Handbook of Chemistry and Physics, 86th edition 2005*; CRC Press, 1998.
(50) Khanuja, M.; Mehta, B. R.; Agar, P.; Kulriya, P. K.; Avasthi, D. K. Hydrogen induced lattice expansion and crystallinity degradation in palladium nanoparticles: Effect of hydrogen concentration, pressure, and temperature. *J. Appl. Phys.* **2009**, *106* (9), 093515.
(51) Bugaev, A. L.; Guda, A. A.; Lazzarini, A.; Lomachenko, K. A.; Groppo, E.; Pellegrini, R.; Piovano, A.; Emerich, H.; Soldatov, A. V.; Bugaev, L. A.; et al. In situ formation of hydrides and carbides in palladium catalyst: When XANES is better than EXAFS and XRD. *Catal. Today* **2017**, *283*, 119−126.
(52) Liu, W.; Magnin, Y.; Förster, D.; Bourgon, J.; Len, T.; Morfin, F.; Piccolo, L.; Amara, H.; Zlotea, C. Size-dependent hydrogen trapping in palladium nanoparticles. *J. Mater. Chem. A* **2021**, *9* (16), 10354−10363.
(53) Ziemecki, S. B.; Jones, G. A.; Swartzfager, D. G.; Harlow, R. L.; Faber, J. Formation of interstitial palladium-carbon phase by interaction of ethylene, acetylene, and carbon monoxide with palladium. *J. Am. Chem. Soc.* **1985**, *107*, 4547−4548.
(54) Tanuma, S.; Powell, C. J.; Penn, D. R. Calculations of electron inelastic mean free paths. V. Data for 14 organic compounds over the 50−2000 eV range. *Surf. Interface Anal.* **1994**, *21* (3), 165−176.
(55) Shinotsuka, H.; Tanuma, S.; Powell, C. J.; Penn, D. R. Calculations of electron inelastic mean free paths. X. Data for 41 elemental solids over the 50 eV to 200 keV range with the relativistic full Penn algorithm. *Surf. Interface Anal.* **2015**, *47* (12), 1132.
(56) Viola, A.; Chattot, R.; Martin, V.; Tsirlina, G.; Nelayah, J.; Drnec, J.; Maillard, F. Hydrogen Trapping in Palladium Nanoparticles Revealed by Electrochemical, X-ray Scattering, and Spectrometric Measurements. *J. Phys. Chem. C* **2023**, *127* (36), 17761−17769.
(57) Alekseeva, S.; Strach, M.; Nilsson, S.; Fritzsche, J.; Zhdanov, V. P.; Langhammer, C. Grain-growth mediated hydrogen sorption kinetics and compensation effect in single Pd nanoparticles. *Nat. Commun.* **2021**, *12* (1), 5427.
(58) Jose, D.; Jagirdar, B. R. Nature of hydrogen atom trapped inside palladium lattice. *Int. J. Hydrogen Energy* **2010**, *35* (13), 6804−6811.
(59) Benck, J. D.; Jackson, A.; Young, D.; Rettenwander, D.; Chiang, Y.-M. Producing High Concentrations of Hydrogen in Palladium via Electrochemical Insertion from Aqueous and Solid Electrolytes. *Chem. Mater.* **2019**, *31* (11), 4234−4245.
(60) Lee, E.; Lee, J. M.; Koo, J. H.; Lee, W.; Lee, T. Hysteresis behavior of electrical resistance in Pd thin films during the process of absorption and desorption of hydrogen gas. *Int. J. Hydrogen Energy* **2010**, *35* (13), 6984−6991.

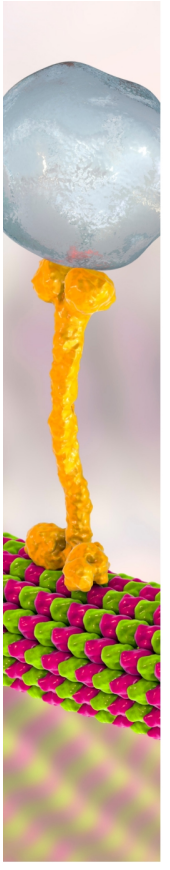

https://doi.org/10.1021/acs.jpcc.5c02040
J. Phys. Chem. C 2025, 129, 13312−13321